RSC Advances

PAPER

View Article Online
View Journal | View Issue

CrossMark click for updates

Cite this: *RSC Adv.*, 2014, **4**, 33911

A facile, morphology-controlled synthesis of potassium-containing manganese oxide nanostructures for electrochemical supercapacitor application†

Navaladian Subramanian, Balasubramanian Viswanathan* and Thirukkallam K. Varadarajan

Potassium-birnessite (K-OL-1) samples of different morphologies (nanowire networks, nanoparticles and mesoporous hierarchical nanowire networks) and textural properties were synthesized from $KMnO_4$ by using oxalate-reduction method under ambient conditions. Cryptomelane (K-OMS-2) samples of similar morphologies were synthesized by the calcination of birnessite samples. The synthesized MnO_2 samples were characterized by XRD, TGA, DTA, SEM, TEM, nitrogen adsorption–desorption and ICP-OES analyses. One each of the birnessite and the cryptomelane samples showed mesoporous nature (pore size ~50 Å and 66 Å respectively). The pH of the reaction medium has been found to have a key role in the properties of the resulting MnO_2 samples. Electrochemical studies of MnO_2–carbon black composites were performed in 0.1 M aqueous Na_2SO_4 solution using cyclic voltammetry and galvanostatic charge–discharge cycling. One of the birnessite samples with nanowire network morphology and a BET surface area of 202 $m^2\ g^{-1}$ exhibited a high capacitance value of 234 F g^{-1}. Electrochemical studies revealed that the specific capacitance values of the studied MnO_2 materials have a direct relationship with their BET surface area values. Birnessite samples have exhibited better capacitance behavior and values than their cryptomelane derivatives. The effect of the morphology has also been reflected in the values of the specific capacitance.

Received 2nd June 2014
Accepted 22nd July 2014

DOI: 10.1039/c4ra05227g

www.rsc.org/advances

Published on 23 July 2014. Downloaded by University of Pittsburgh on 30/10/2014 17:09:27.

1. Introduction

In recent times, the development of alternative energy conversion/storage devices with high power and energy densities has gained importance due to the depletion of fossil fuels.[1] Electrochemical capacitors have received enormous attention owing to their higher power density and longer cycle life as compared to secondary batteries. Moreover, electrochemical capacitors exhibit higher energy density than conventional electrical double-layer capacitors.[2,3] In particular, electrochemical capacitors based on hydrous ruthenium oxides exhibit higher specific capacitance than conventional carbon materials and better electrochemical stability than electronically conducting polymer materials.[4] However, the high cost of noble metal-based materials limits them from commercialization. Hence, emphasize has been made in searching for alternative but inexpensive electrode materials with good capacitive characteristics, such as NiO, CoO_x, MnO_2, V_2O_5, WO_x, MoO_x *etc.*[5–11]

Manganese oxides are important and well-studied class of materials in the fields of catalysis, ion-exchangers, molecular adsorption, biosensors, batteries, electrochemical capacitors, oxygen reduction (in fuel cells) and solar materials.[12–19] Due to the low cost and that MnO_2 forms variety of structures, MnO_2-based materials have been anticipated as potential replacement for hydrous RuO_2. The simple electrochemical double layer capacitance (EDLC) process is a non-Faradaic process attributed to charge separation at the electrode/electrolyte interface whereas the pseudocapacitive (Faradaic) process depends on redox reactions that occur in the bulk of the electrode materials as well. Hence, pseudocapacitors exhibit higher capacitance than the EDLC.[3] There have been two mechanisms proposed to explain the charge storage behavior of MnO_2 as an active electrode material in aqueous electrochemical supercapacitor.[20] The first mechanism is based on the surface adsorption of protons (H^+) or electrolyte cations (M^+) on MnO_2 (eqn (1)) and the second one involves the intercalation of protons (H^+) or alkali metal cations (M^+) such as Na^+ in the bulk of the material upon reduction or deintercalation upon oxidation (eqn (2)).[21,22]

Department of Chemistry, National Centre for Catalysis Research, Indian Institute of Technology Madras, Chennai 600 036, India. E-mail: bvnathan@iitm.ac.in; Tel: +91 44 2257 4241

† Electronic supplementary information (ESI) available: XRD powder patterns of Crypt-(A, B and C) 800(2h), SEM image and EDS of Crypt-C600, TEM image of Crypt-C400 and Crypt-A600, low angle XRD powder pattern of Birn-C and Horvath–Kawazoe pore size distributions of birnessite and cryptomelane samples. See DOI: 10.1039/c4ra05227g

Published on 23 July 2014. Downloaded by University of Pittsburgh on 30/10/2014 17:09:27.

The first mechanism is predominant in the case of amorphous MnO_2 materials whereas the second mechanism is predominant in the case of crystalline MnO_2 materials.

$$(MnO_2)_{surface} + M^+ + e^- \leftrightarrows (MnO_2^-M^+)_{surface} \quad (1)$$

$$MnO_2 + M^+ + e^- \leftrightarrows MnOOM \quad (2)$$

where M^+ can be Li^+, Na^+, K^+ or H_3O^+.

Hence, capacitance of MnO_2 depends on crystal structure, ionic conductivity, size of the cavity (of tunnel and layers), morphology and textural properties such as surface area, pore size and pore volume.[23–26] So, open structures of MnO_2 such as layered and tunneled ones are more preferred for the fast ionic transportation into the bulk of the electrode material in order to achieve high capacitance.

MnO_2 exists in several crystallographic forms such as α-, β-, γ-, δ-, λ- and ε-type, because the basic unit [MnO_6] octahedron links in different ways. In particular, δ-, α-MnO_2 and OMS-5 forms are of much interest in view of their good electrochemical capacitance behavior due to their large cavity and high ionic conductivity.[23,25,27] Hence, synthesis of birnessite (δ-MnO_2) and cryptomelane (α-MnO_2) with the requisite features for showing high charge storage is of great interest. Birnessite is a layered manganese oxide material comprising layers of edge-shared MnO_6 octahedra, and cations ($A = K^+$, Na^+) and water molecules situated between the negatively charged layers. These materials are known as octahedral layers (A-OL-1) with the interlayer cation (A^+).[28] Cryptomelane is a type of manganese oxide consisting of 2 × 2 edge-shared MnO_6 octahedra chains, which are corner-connected to form one-dimensional tunnels of *ca.* 4.6 × 4.6 Å and the tunnels are stabilized by K^+ ions.[29] Also, the cryptomelane is known as octahedral molecular sieve (K-OMS-2). Schematic structures of K-birnessite and cryptomelane are given in Fig. 1. Potassium-birnessite can be converted into cryptomelane by heat treatment as depicted in Fig. 1.[29]

There has been a variety of methods known for the synthesis of birnessite and it has been synthesized by oxidizing Mn^{2+} by oxygen in presence of KOH, hydrothermal route, or calcination of $KMnO_4$.[30–33] Apart from those methods, chemical reduction of $KMnO_4$ by using reducing agent such as ethanol, glucose, ascorbic acid, fumaric acid, maleic acid, ethylene glycol, or polyvinyl alcohol for obtaining birnessite has also been reported.[22,28,34–36] Cao *et al.* reported the formation of an amorphous manganese oxide (AMO) by randomly mixing $KMnO_4$ and oxalic acid solutions.[37] However, strategic synthesis of birnessites with different morphologies and porosities by varying the rate and the order of mixing of the reactants, $KMnO_4$ and oxalic acid, has not yet been known. This article describes the synthesis of birnessite with three different morphologies and textural properties by the alteration of rate and order of mixing $KMnO_4$ and oxalic acid solutions, their further transformation to cryptomelane of similar morphologies by calcination, and their electrochemical performances for charge storage in 0.1 M aqueous Na_2SO_4 electrolyte.

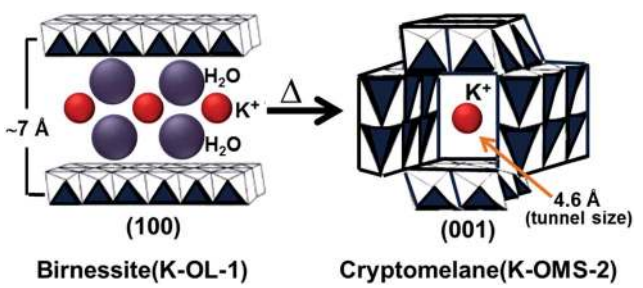

Fig. 1 Schematic of birnessite and cryptomelane structures.

2. Experimental section

2.1. Methods

2.1.1. Synthesis of birnessites. Birnessite samples were synthesized by the chemical reduction of $KMnO_4$ using oxalic acid as a reducing agent under mild conditions. Three different methods (A, B and C) were adopted for the synthesis of birnessites by altering the rate and the order of mixing the reactants of same concentrations.

Method A. To the 100 ml of 15 mM oxalic acid (Merck) solution, 100 ml of 10 mM of $KMnO_4$ (Fluka) solution was added with the rate of 1 ml min^{-1} using a peristaltic syringe pump (Miclines, India) under constant stirring at room temperature. After the complete addition, the obtained black-brown turbid solution was digested at 60 °C for 30 min. The brown precipitate obtained was washed by centrifugation with doubly distilled water and dried at 120 °C for 6 h. The dried powder was brittle and the as-synthesized sample is denoted as Birn-A.

Method B. This method is similar to method A except that oxalic acid solution was added to $KMnO_4$ solution with the rate of 1 ml min^{-1}. Thus, the order of the addition is reversed. After the reaction, a brown colloid formation was observed, which was not settling down even after digestion. The dried powder was brittle and the as-synthesized sample is denoted as Birn-B.

Method C. This method is similar to the method-A except that both the reactants were mixed together all at once to get the precipitate. Thus, the rate of mixing the reactants is varied. After mixing the reactants, the reaction was vigorous with effervescence to yield a black gel, which was settling down easily. After drying, the obtained xerogel was hard to be ground and the as-synthesized sample is denoted as Birn-C.

2.1.2. Synthesis of cryptomelanes. Different cryptomelane samples were obtained by calcining Birn-A, Birn-B and Birn-C at 400 °C for 2 or 4 h, or 600 °C for 4 h in air. The resulting cryptomelane samples are denoted as Crypt-A, Crypt-B and Crypt-C with the temperature but devoid of unit (°C). Unless otherwise mentioned, the period of calcination is 4 h.

2.2. Characterization

Powder X-ray diffraction (XRD) patterns of all K–MnO_2 samples were recorded using Rigaku MiniFlex2 diffractometer at a scan rate of 0.1° s^{-1} with Ni-filtered Cu K_α radiation ($\lambda = 1.5406$ Å) as the X-ray source. Thermo gravimetric analysis (TGA) and differential thermal analysis (DTA) of birnessite samples were performed with PERKIN-ELMER TGA (Delta series TGA7)

 This journal is © The Royal Society of Chemistry 2014

Published on 23 July 2014. Downloaded by University of Pittsburgh on 30/10/2014 17:09:27.

instrument at a heating rate of 10 °C min^{-1} in air atmosphere. Nitrogen adsorption–desorption experiments were carried out using a Micrometrics ASAP 2010 accelerated surface area system. The nitrogen adsorption and desorption experiments were carried out at 77 K with samples previously degassed at 150 °C for 12 h. Specific surface areas of the samples were determined by the Brunauer–Emmett–Teller (BET) method. Micropore and mesopore size distributions were calculated by Horvath–Kawazoe (HK) and Barrett–Joyner–Halenda (BJH) methods respectively.

Manganese and potassium contents in K–MnO_2 samples were analyzed by inductively coupled plasma-optical emission spectra (ICP-OES) using PERKIN-ELMER OPTIMA 5300 DV ICP-OES system. Samples were dissolved in 1% HCl and emission of K and Mn was monitored at 766.49 nm and 257.6 nm respectively. Average oxidation state (AOS) of Mn was determined using a two-step procedure described previously.[38] The samples were dissolved in H_2SO_4 solution and Mn^{3+} as well as Mn^{4+} was reduced to soluble Mn^{2+} using Fe^{2+}. Titrations of the resulting Mn^{2+} and the excess of Fe^{2+} were carried out to determine the AOS. Scanning electron micrographs were recorded using FEI QUANTA FEG 200 scanning electron microscope operating at 30 kV. Transmission electron micrographs (TEM) were recorded with PHILIPS CM12 and JEOL-3010 transmission electron microscopes operating at 100 kV and 300 kV respectively. Samples for TEM analyses were prepared by dispersing them in ethanol by sonication followed by drop-drying on copper grids coated with carbon film.

Electrochemical performance of MnO_2–ketjen black carbon composites was studied using cyclic voltammetry curves and charge–discharge curves. Ketjen black carbon was used as a conducting additive. Fabrication of electrodes for electrochemical studies was done as follows. In a typical procedure, 75 wt% of MnO_2, 20 wt% of ketjen black EC-600 JD and 5 wt% of polyvinylidene fluoride (PVDF) were mixed by mild grinding. From the mixture, 10 mg of solid mass was taken and dispersed in 0.25 ml of doubly distilled water in a vial by ultrasonication. From the colloid, a volume of 10 μl was transferred to polished glassy carbon surface and dried at 60 °C to get the semisolid of the composite for electrochemical studies. Electrochemical studies were performed in 50 ml of 0.1 M aqueous sodium sulphate solution. Cyclic voltammograms were recorded at a scan rate of 10 mV s^{-1} in the potential range of 0 to 1 V and galvanostatic charge–discharge cycles were collected with a current of 0.5 mA. The cyclic voltammetry and galvanostatic charge–discharge experiments were performed using a CHI 660A (CH Instruments, USA) electrochemical work station. A conventional three-electrode cell consisting of a polished glassy carbon (GC) (0.07 cm^2) working electrode, a Pt foil (5 cm^2) counter electrode and a Ag/AgCl (Satd. KCl) reference electrode was used for the electrochemical studies of MnO_2–carbon composites.

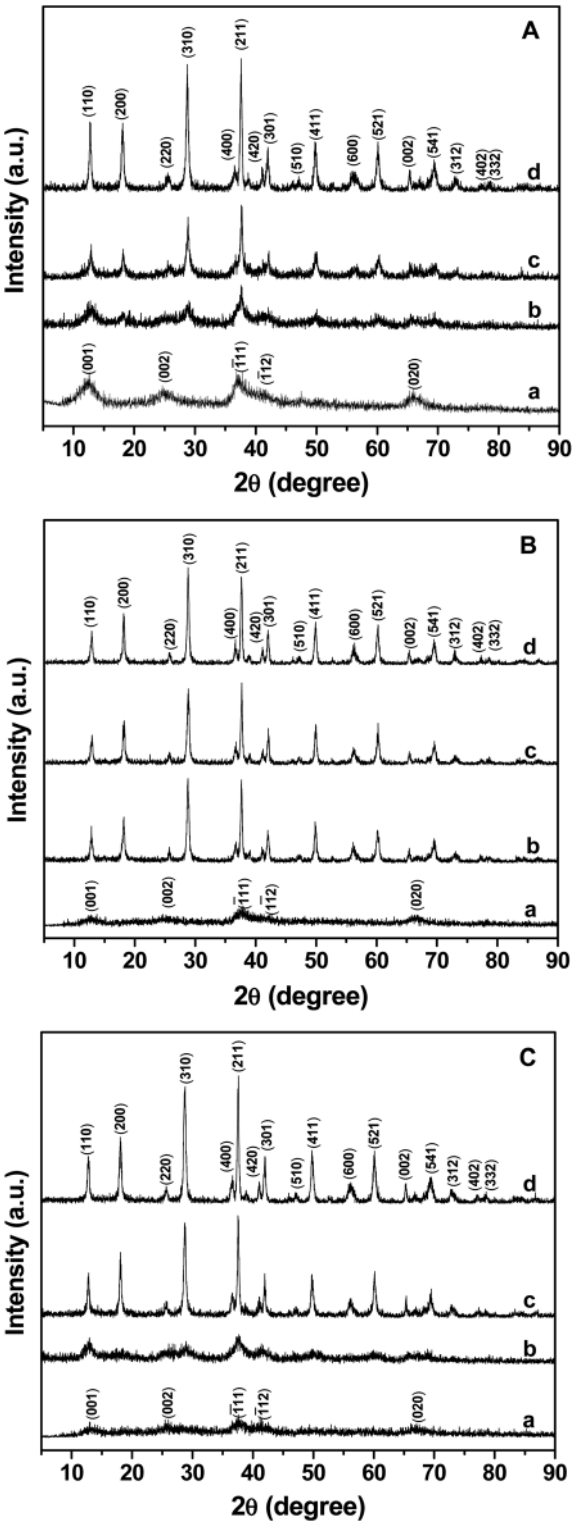

Fig. 2 Powder XRD patterns of birnessites and cryptomelanes and A, B or C denotes the method of preparation. (a) Birnessite; (b) Crypt-400(2h); (c) Crypt-400; (d) Crypt-600.

3. Results and discussion

3.1. Powder XRD studies

Powder XRD patterns of birnessite and cryptomelane samples are given in Fig. 2A–C and S1.† The broad peaks with low intensities in XRD patterns of the as-synthesized samples reveal the poor crystalline nature of the birnessites. Crystallinity of the birnessites is in the following order: Birn-A > Birn-B > Birn-C. XRD patterns clearly reflect the typical feature of layered compounds with a turbostratic disorder.[39,40] In other words, the

Published on 23 July 2014. Downloaded by University of Pittsburgh on 30/10/2014 17:09:27.

sample consists of layers arranged parallel and equidistant without a well-defined displacement/rotation between the successive layers.[41] XRD patterns of as-synthesized samples show five diffraction peaks, which can be indexed to the end-centered monoclinic potassium birnessite (JCPDS file no. 80-1098). The first two diffraction peaks with d value around 7 Å and 3.5 Å correspond to (001) and (002) basal reflections, while the three asymmetric broad peaks with $d = 2.4$, 1.4, and 1.2 Å are indexed to (20l; 11l), (02l; 31l), and (22l; 40l) diffraction bands, respectively.[39,40] The d_{001} values of Birn-A, Birn-B and Birn-C are 6.94, 6.94 and 6.8 Å respectively and these d values corresponds to the interlayer spacings, characteristic of the birnessite intercalated with K^+ ions and H_2O molecules. The week intensity of (001) and (002) reflections observed in the case of Birn-B indicates the presence of orientation of *ab*-plane in it.

Reflections of XRD pattern of cryptomelanes obtained by calcining birnessite samples at 400 °C for 4 h and 600 °C for 4 h are indexed to tetragonal body centered lattice with the space group $I4/m$ and lattice constants $a = 9.784$ Å and $c = 2.2863$ Å (JCPDS no. 44-0141). However, birnessites calcined at 400 °C for 2 h show only a few reflections of cryptomelane as compared to Crypt-400 samples. This shows that the calcination for 2 h is not sufficient for the formation of cryptomelane, especially for Birn-A and Birn-C. As per the intensity of the XRD lines, the crystalline nature of cryptomelanes obtained by the calcination at 400 °C for 2 h is in the following order; Crypt-B > Crypt-A > Crypt-C. This observation implies that Birn-B is transformed into cryptomelane in a more facile manner than A and C analogues. This kind of easy phase transformation observed with Crypt-B400(2h) may be attributed to lower stability, which in turn attributed to the lesser potassium content in Birn-B.[42] XRD patterns of cryptomelanes obtained by the calcination at 800 °C for 2 h are given in Fig. S1.† The presence of XRD lines corresponding to only cryptomelanes proves that no further phase transition occurred even by the calcination at 800 °C for 2 h. The XRD results prove that the cryptomelanes synthesized by this method are thermally stable even at 800 °C.

3.2. TG/DTA, AOS and ICP analyses

TGA, DTG and DTA profiles of birnessites are given in Fig. 3. In the TGA profiles, initial weight loss below 120 °C is attributed to the removal of physisorbed water and further weight loss above 120 °C is due to the dehydration of layers of birnessite. Weight loss corresponding to the water removal observed between 100 and 250 °C for Birn-A, Birn-B or Birn-C is 8.1, 5.4 or 5.1% respectively. The subsequent weight loss observed in the range of 300–480 °C is attributed to the removal of lattice oxygen. This loss of oxygen takes places due to the reduction of a fraction of Mn(IV) ions to Mn(III) ions. In the case of Birn-A, Birn-B or Birn-C, the weight loss with regard to loss of oxygen is 2.3, 2.1 or 2.8% respectively. Slight weight gains of 1.6 and 0.6% observed respectively for Birn-B and Birn-C after 480 °C are due to the uptake of oxygen during the phase transformation of birnessite to cryptomelane.[43,44] The weight gain observed after 498 °C for Birn-B is 40 °C lower than for Birn-C. This is in agreement with DTA results where endothermic peaks corresponding to the phase transition of layered to tunneled MnO_2 are observed at 498 and 536 °C respectively for Birn-B and Birn-A. This phase transformation at lower temperature shown by Birn-B is probably due to the lower thermal stability of birnessite phase, which in turn due to its lower K content.[42] However, Birn-A does not show any weight gain after 480 °C but shows an endothermic peak in DTA corresponding to the phase transition that occur at 536 °C without any reduction of Mn(IV). The low

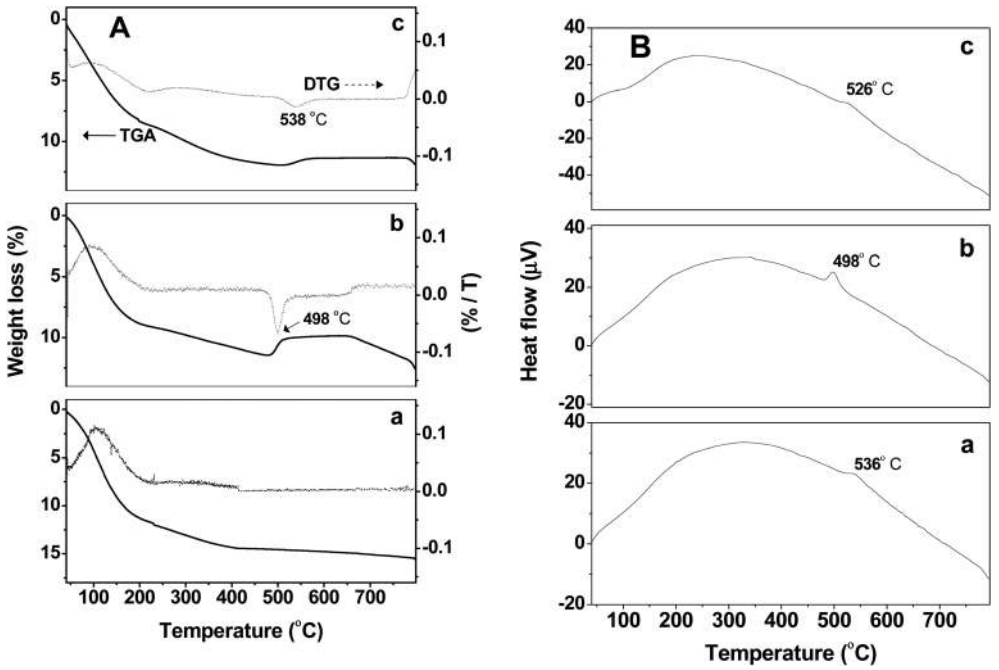

Fig. 3 TGA (A) and DTA (B) profiles of birnessite samples recorded in air atmosphere. (a) Birn-A; (b) Birn-B; (c) Birn-C.

 This journal is © The Royal Society of Chemistry 2014

Published on 23 July 2014. Downloaded by University of Pittsburgh on 30/10/2014 17:09:27.

Table 1 Average oxidation state (AOS), K–Mn ratio, textural properties and capacitance of birnessite and cryptomelane samples

Sample	AOS	K/Mn	BET surface area (SSA) ($m^2\ g^{-1}$)	*t*-Plot surface area ($m^2\ g^{-1}$)	Pore volume ($cm^3\ g^{-1}$) (BET)	Micro pore volume ($cm^3\ g^{-1}$) (*t*-plot)	Pore size (Å) (BJH)	Specific capacitance (C_s) (F g^{-1}) from CD curves	C_s/SSA F m^{-2}
Birn-A	3.68	0.140	202	28	0.51	0.014	101	234	1.158
Birn-B	3.81	0.099	133	18	0.33	0.0093	—	113	0.849
Birn-C	3.72	0.126	186	14	0.22	0.0069	50	201	1.080
Crypt-A400	3.71	0.124	136	22	0.57	0.011	196	137	1.007
Crypt-B400	3.85	0.101	40	4.5	0.17	0.0021	—	33	0.825
Crypt-C400	3.76	0.113	130	15	0.22	0.0073	66	128	0.985

temperature phase transition shown by Birn-B is in good agreement with XRD patterns, wherein the clear peaks of cryptomelane were observed even in the case of 2 h calcination at 400 °C.

The average oxidation state (AOS) of manganese and K : Mn ratio of both birnessites and cryptomelanes are given in Table 1. As for birnessites, the AOS of Mn is in the range of 3.68 to 3.81 and Birn-B shows the highest AOS. A similar trend is observed in the case of cryptomelanes as well. These values imply the presence of both Mn(IV) and Mn(III) ions in both birnessites and cryptomelanes.[33] However, the AOS is found to be slightly higher for cryptomelanes. This increase in the AOS of Mn is attributed to the oxidation of residual Mn(III) to Mn(IV) during the calcination in air atmosphere at 400 °C. The K : Mn ratios of Birn-A, Birn-B and Birn-C are in the range of 0.1 to 0.14. This observation with potassium content of birnessite samples has good correlation with XRD and TGA results where Birn-B is revealed to undergo phase transition at low temperatures than Birn-A and Birn-C. This lower K : Mn ratio might be due to the lower K : Mn of 1 : 1 in $KMnO_4$ precursor. It is known from the literature that only 10% of the initial K^+ was incorporated into MnO_2 in the case of birnessites synthesized by the chemical reduction of $KMnO_4$.[45] The slightly lower K : Mn ratio of cryptomelane samples than their precursor birnessite samples is probably due to the loss of potassium that occurred during the calcination followed by washing with deionized water prior to the estimation by ICP analysis. This loss of K may be attributed to the expulsion of K^+, which in turn due to the space shrinkage that takes place during the phase-transition of layered MnO_2 to tunneled one.[42]

3.3. Electron microscopic analysis

SEM images of birnessite and Crypt-(A, B and C)400 samples are given in Fig. 4 and 5 respectively. Birn-A (in Fig. 4a) shows aggregates of particles without any specific morphology. However, Birn-B shows aggregates of separate particles of size ranging from ~10 to ~60 nm while Birn-C exhibits bulk particles appearance. SEM image of Crypt-A400 shows the presence of bunch of nanorods along with aggregates of particles. However, Crypt-B400 (Fig. 5b) exhibits the presence of individual particles similar to Birn-B. Crypt-C400 exhibits the morphology similar to that of Crypt-A400 (Fig. 5c) but is denser than Crypt-A400. In the case of Crypt-C600 (Fig. 5d and S2†), presence of hierarchical nanowires network structure is observed and the average size of the nanowires is 45 nm. EDS of

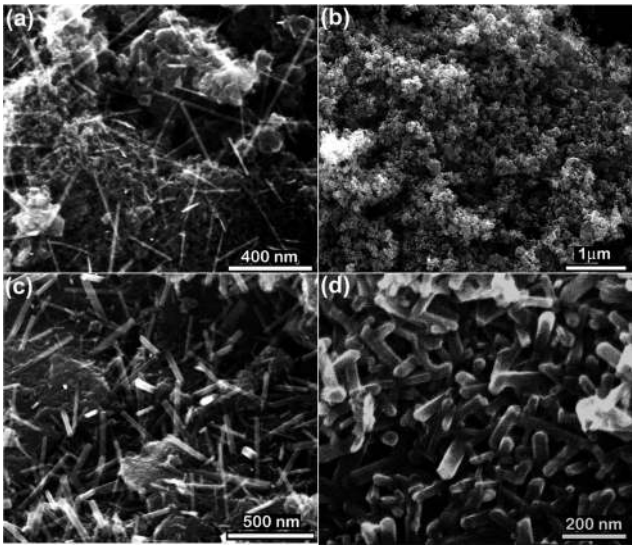

Fig. 5 SEM images of cryptomelane samples. (a) Crypt-A400; (b) Crypt-B400; (c) Crypt-C400; (d) Crypt-C600.

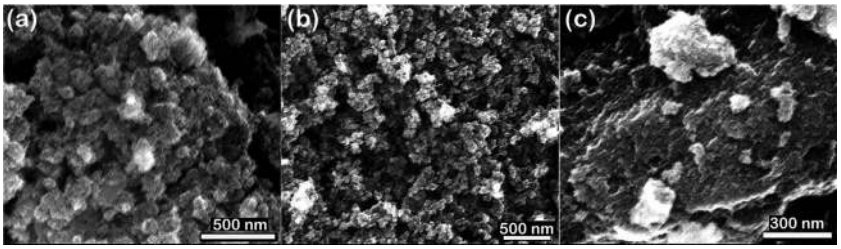

Fig. 4 SEM images of birnessite samples. (a) Birn-A; (b) Birn-B; (b) Birn-C.

Published on 23 July 2014. Downloaded by University of Pittsburgh on 30/10/2014 17:09:27.

Crypt-C600 recorded during SEM analysis is provided in Fig. S3† and the presence of the peaks corresponding to oxygen, potassium and manganese confirms that the sample is K-containing manganese oxide.

HRTEM images of Birn-A are given in Fig. 6. HRTEM images of two different magnifications in Fig. 6a and b show the presence of particles with gel-type (porous) or fluffy appearance. Lattice-resolved HRTEM image in Fig. 6c shows projecting nanofibers of thickness ~3 nm with lattice fringes thickness of 6.2 Å. However, thickness of lattice fringes is not found to be uniform and varies from 6.2 to 7.6 Å.[46] These lattice fringes correspond to the d_{001} of end centered monoclinic birnessite lattice. This observation indicates that MnO_6 octahedral layers are seen across the nanofibers, which in turn implies that growth of nanofibers has occurred along (100) facet of the birnessite lattice. The observed variable d_{001} of lattice fringes implies the poor crystalline nature of birnessite as observed in XRD pattern. Even in a same nanofiber, d_{001} is not uniform throughout the fiber. This may be due to the non-uniform K^+ ion incorporation in between the layers, which in turn may be due to lower K content in the material. Moreover, some of the nanofibers are found to contain as low as four layers.

TEM images of cryptomelane samples are given in Fig. 7. TEM image of Crypt-A400 given in Fig. 7(a) shows the bunch of nest-like nanorods network of cryptomelane. Thicknesses of the nanorods are in the range of 8 to 20 nm and the length is up to ~1 μm. TEM image of Crypt-B400 show the presence of pseudo-spherical particles of size that is ranging from ~15 nm to ~60 nm. TEM image of Crypt-C400 in Fig. 7(c) and S4† shows porous gel-type network of nanorods. Projection of nanorods (shown with arrows) in the periphery of the nest-like aggregate is seen and thickness of those nanorods is ~20 nm. SAED pattern recorded on the aggregates shows rings, which are indexable to (220), (310), (301), (411) and (521) reflections of cryptomelane lattice.

HRTEM images of Crypt-A600 are given in Fig. 8. Low magnification HRTEM image in Fig. 8a shows the presence of nanorods of length up to few μm and thickness of the nanorods varies from 5 to 50 nm. HRTEM image of an edge of a nanorod of Crypt-A600 and its lattice-resolved image (inset) are given shown in Fig. 8b. Thickness of the nanorod is around 48 nm and the d value of the lattice fringes is 4.9 Å. This d value corresponds to {200} planes of the cryptomelane, revealing that growth of the nanorod has occurred along [100]. TEM image in Fig. 8c shows edges of the nanorods of thickness of ~42 nm. The lattice-resolved image in Fig. 8d depicts the edge of the nanorod and the corresponding lattice fringes show the d value of 7 Å. This d value reveals that the lattice fringes correspond to {110} planes of cryptomelane and indicates that growth direction of the nanorod is [110]. This contradictory observation found between two different nanorods regarding lattice alignment implies that nanorod growth occur along [100] or [110] direction. TEM images of Crypt-A600 given in Fig. S5† show bundles of nanorods. This type of bundling might arise from the side-on fusion of nanorods occurred by oriented attachment during the heat treatment.[38,47]

HRTEM images of Crypt-B600 are given in Fig. 9. Low magnification image in Fig. 9(a) shows nanoplates, short nanorods and spherical particles. Sizes of the nanoparticles are in the range of 15 to 60 nm. Fig. 9(b) shows a lattice-resolved

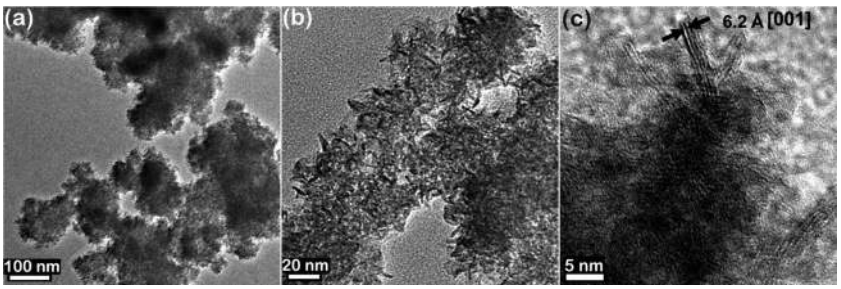

Fig. 6 HRTEM images of Birn-A. (a) and (b) low magnification and (c) lattice-resolved TEM images of Birn-A.

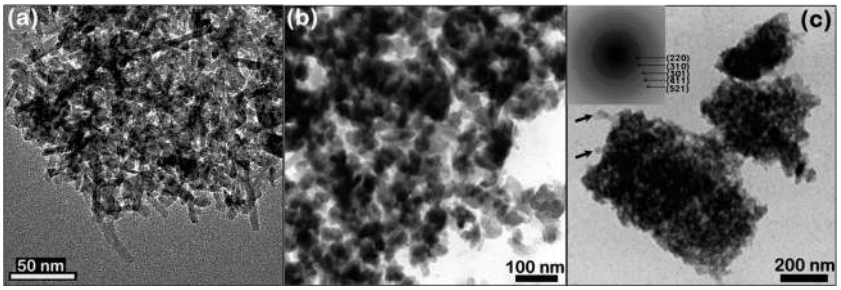

Fig. 7 HRTEM image of Crypt-A400 (a) and TEM images of Crypt-B400 (b) and Crypt-C400 (c). Inset in image (c) shows SAED pattern acquired on Crypt-C400, and arrow marks indicate the projecting nanorods.

 This journal is © The Royal Society of Chemistry 2014

Published on 23 July 2014. Downloaded by University of Pittsburgh on 30/10/2014 17:09:27.

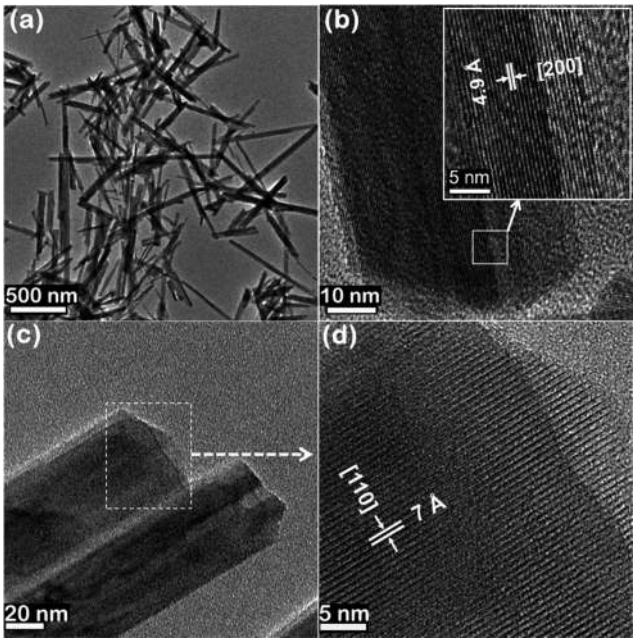

Fig. 8 HRTEM images of Crypt-A600. (a) low magnification image; (b) TEM image of a nanorod and its lattice-resolved image of a side portion (inset); (c) TEM image of edges of nanorods; (d) lattice-resolved TEM image of an edge of the nanorod in (c).

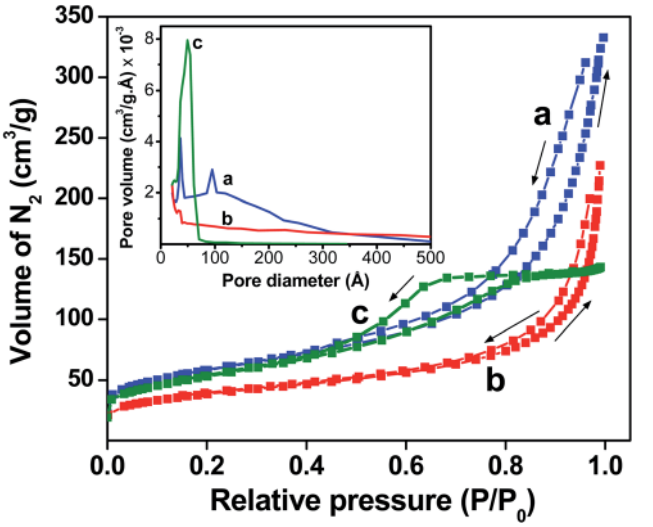

Fig. 10 Nitrogen adsorption–desorption isotherms of (a) Birn-A, (b) Birn-B and (c) Birn-C. Inset shows the BJH pore size distributions.

image of a couple of nanoplates and thicknesses of the lattice fringes are 7 Å and 4.9 Å. These lattice fringes correspond to {110} and {200} respectively. This implies that top and basal planes of nanoplates are {001} plane of cryptomelane lattice. Lattice-resolved HRTEM image of the nanoparticle in Fig. 9(c) shows lattice fringes corresponding to d_{200} of cryptomelane.

3.4. Nitrogen adsorption–desorption isotherm and surface area analysis

Nitrogen (N_2) adsorption–desorption isotherm and BJH pore size distribution of birnessites and cryptomelanes obtained by calcination at 400 °C for 4 h are given in Fig. 10 and 11 respectively. Birn-A, Birn-B, Crypt-A400 and Crypt-B400 show Type II adsorption isotherm with micropore filling at low P/P_0 values, capillary condensation at high P/P_0 values and H3 hysteresis.[48] However, these features indicate the presence of micropores, slit-like mesopores and macropores formed by the particles (interparticle pores) in the samples. Birn-C and Crypt-C400 exhibit Type IV isotherm with H2 hysteresis loop, indicating the presence of cylindrical mesopores with bottle shape (narrow mouth).[49] However, absence of peaks in low angle XRD pattern (in Fig. S6†) reveals the absence of ordered mesoporous nature and that mesoporosity arises from the interparticle pores generated by the hierarchical network of nanorods as observed in SEM image. BET surface area, *t*-plot microporous surface area and pore volume of the samples are given in Table 1. Birn-A and Birn-B show the wide distribution of pore size. Average pore size of Birn-A is found to be ~100 Å. In contrast, no sharp pore size is observed in the case of Birn-B. The pore size distribution of Birn-C is found to be narrow as evidenced by H3 hysteresis and its average pore diameter is ~50 Å. However, the average pore size has been increased in the case of Birn-C upon calcination. This may be due to the phase transition of birnessite to cryptomelane. BET surface area of birnessite samples is in the following order: Birn-A > Birn-C > Birn-B. Among all, Birn-A shows the highest surface area of 202 $m^2\ g^{-1}$. BET surface areas of birnessite samples are higher than that of cryptomelane samples. There is a drastic reduction of surface area that occurred during the transformation of Birn-B to crypt-B400. This may be due to the sintering and the phase transition

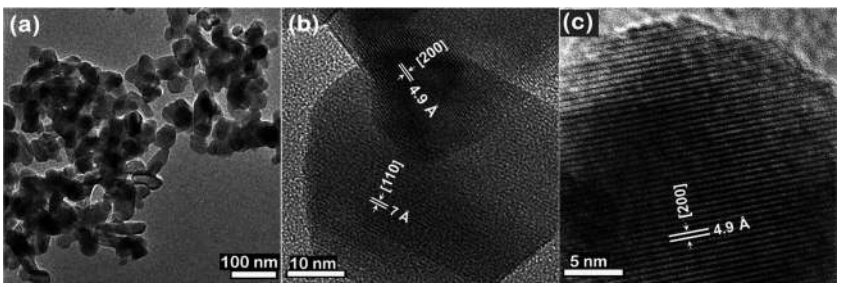

Fig. 9 HRTEM images of Crypt-B600. (a) Low magnification image; (b) and (C) lattice-resolved images of nanoplates and a nanoparticle respectively.

Published on 23 July 2014. Downloaded by University of Pittsburgh on 30/10/2014 17:09:27.

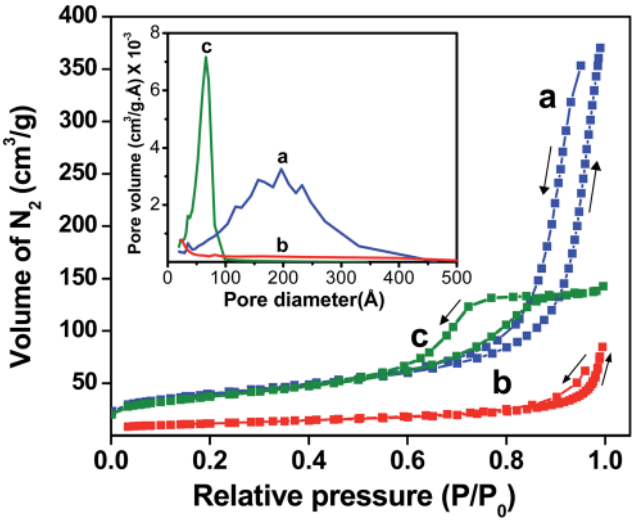

Fig. 11 Nitrogen adsorption–desorption isotherms of (a) Crypt-A400, (b) Crypt-B400, and (c) Crypt-C400. Inset shows BJH pore size distributions.

occurring during the heat treatment. Due to the sintering, some of the pores might have closed.

As for BET surface area, the trend of cryptomelanes is similar to that of birnessite samples. In general, surface area calculated using *t*-plot is indicative of the surface area that arises due to micropores. Birn-A and Crypt-A400 exhibit microporous surface area of 28 and 22 $m^2\ g^{-1}$ respectively, which are higher than that of B and C analogues of birnessite and cryptomelane. Microporous surface area of Birn-B decreased drastically when it was transformed to Crypt-B400. Microporous surface area of Birn-C is only 14 $m^2\ g^{-1}$ and it is maintained even after the transformation into cryptomelane. Pore volume of Birn-A is higher than that of Birn-B and Birn-C due to the wide range of pore sizes exhibited by the former. Upon transition into Crypt-A400, the pore volume increases for Birn-A due to the increase in the pore size. However, in the case of both Birn-C and Crypt-C400, the pore volume remains the same even though the pore size increases from 50 to 66 Å. This phenomenon is mainly attributed to the effect of morphology. During sintering, crystallographically identical planes fuse (oriented attachment) to give rise to bigger particles and hence alignment of particles (or rods) is significant.[38,47] The favorable alignment of the particles is less likely in the case of Birn-C because the nanorods are thickly packed, unlike Birn-A.[47] Birn-B, on the contrary, show high degree of sinteing to form bigger particles due to its non-1 D morphology, that provides more freedom for favorable alignment than the rod morphology. In Fig. S7 and S8,† Horvath–Kawazoe micropore size distributions of birnessites and cryptomelanes are given as it is a reliable indicator of micropore size distribution of materials. The average micropore size lies below 10 Å for birnessites and cryptomelanes. The differences in the textural properties observed among cryptomelanes are mainly attributed to the morphology and the associated alignment of their birnessite precursor particles.

3.5. Mechanism of formation

Formation of manganese oxide precipitate occurs by the stoichiometric reaction between aqueous solutions of $KMnO_4$ and oxalic acid as shown in eqn (3).

$$2KMnO_4 + 3H_2C_2O_4 \rightarrow 2MnO_2\downarrow + 6CO_2\uparrow + 2KOH + 2H_2O \quad (3)$$

This reaction is more favorable even at room temperature due to the favorable standard reduction potentials of potassium permanganate and oxalic acid. The corresponding standard reduction potentials are $E^o(MnO_4^-/MnO_2^-, 2OH^-) = 1.679$ V and $E^o(2CO_2/C_2O_4^{2-}) = -0.49$ V.[50,51] During the reaction, gas evolution was observed and the gas was tested by dipping the outlet of the reaction in baryta solution (10% $Ba(OH)_2$ in water). Formation of white precipitate was observed while the outlet gas was purged through baryta, confirming the CO_2 evolution from reaction medium to form $BaCO_3$ (white precipitate).[52] As understood from the eqn (3), pH of the solution after the completion of reaction was found to be alkaline (pH ≈ 9.6). In general, this reduction reaction is fast only in the acidic medium because H^+ is consumed in this reaction.[53] In addition, there was no reaction occurring when potassium oxalate was used in place of oxalic acid. After the reduction of MnO_4^- by oxalic acid, formation of MnO_x is observed. Further, it polymerizes to form edge-shared MnO_6 octahedral layers in the presence of K^+ ions in neutral or acidic medium under mild conditions to form birnessites. Formation of crystalline birnessites occurs only in highly alkaline solutions at high temperature or under hydrothermal conditions.[28,32,35,40,54,55] Hence, birnessite formed in the current synthesis is amorphous.

In order to understand the effect of pH, a separate set of experiments was carried out by measuring pH of reaction medium after 5 min of addition of every 10 ml of reactants. In method A, the initial pH of ~3.4 was increasing gradually to 9.64 (after the complete addition). The colloid formation was observed only after addition of 40 ml of $KMnO_4$ (pH ≈ 5.1). This implies that the nucleation and particle growth take place at acidic condition. Further, addition of $KMnO_4$ generates MnO_x units, which stack over the birnessite nuclei crystallite to give rise to the formation of fibers of birnessite. So is the case with method C except that the growth rate is faster in method C (due to the mixing of reactants all at once). Therefore, formation of thickly-packed nanorods (a gel-type) with uniform pore size has been observed. However, initial and final pH values were 8.7 and 9.6 respectively in the case of method B and pH has not reduced below 7.3 throughout the addition of oxalic acid. And, appearance of colloid was observed only after the addition of 80 ml (pH ≈ 8.1). This implies that homogenous nucleation followed by the fast particle growth occur in alkaline medium. Hence, formation of only non-spherical particles or plates is observed in the case of method B.[20,28,32,53–55] Thus, pH plays a major role in the nucleation and the crystal growth and, in turn, in the morphology and the textural properties of the resulting MnO_2. Cryptomelane samples synthesized retain the morphology and the nature of the pore size distribution of their

 This journal is © The Royal Society of Chemistry 2014

Published on 23 July 2014. Downloaded by University of Pittsburgh on 30/10/2014 17:09:27.

birnessite precursor analogues. Based on the results, a schematic of formation of K–MnO_2 material synthesized is presented in Fig. 12.

3.6. Electrochemical studies

Cyclic voltammograms (CV) of carbon composites of birnessites and cryptomelanes (400 °C, 4 h) recorded in 0.1 M aqueous Na_2SO_4 solution are shown in Fig. 13(A) and (B) respectively. Birn-A and Birn-C show rectangular-shaped CV curves indicating the ideal capacitive behavior. However, Birn-B shows oval-shaped CV curve, indicating the poor capacitive behavior at this particular scan rate. The voltage drop observed at the cut off voltages (0 and 1 V *vs.* Ag/AgCl) may be due to the interparticle resistance (contributing to electrode resistance). Birn-A shows the reversible redox peaks in the CV curve in the cathodic and the anodic regions. In the case of cryptomelane-based electrodes, a pair of anodic peaks and a single cathodic peak is observed. These types of redox peaks exhibited by cryptomelanes have been known in the literature.[25,56–60] Pseudocapacitance of MnO_2 in aqueous medium is usually generated by the transitions of interfacial oxycation species at various oxidation states.[61] The redox peaks may reflect the redox transitions of Mn between different valence states, including Mn^{3+}/Mn^{2+}, Mn^{4+}/Mn^{3+}, and Mn^{6+}/Mn^{4+}. Repetitive insertion/extraction processes of Na^+ and K^+ cations into bulk of the material may cause the appearance of various redox peaks in the cyclic voltammograms of cryptomelane. This phenomenon has also been observed in the other tunneled MnO_2 allotropes such as OMS-5 (2×4 tunnels).[25] In both cases, the insertion/extraction process is facilitated by their large cavity sizes.[25,59] Area of the CV curves of the electrodes is directly proportional to the charge, which in turn proportional to the capacitance.[61] As for birnessites, the order of the capacitance is as follows: Birn-A > Birn-C > Birn-B. The same is the order in the case of cryptomelane analogues. This trend of the capacitance of the samples is consistent with the surface area of birnessites and cryptomelanes.

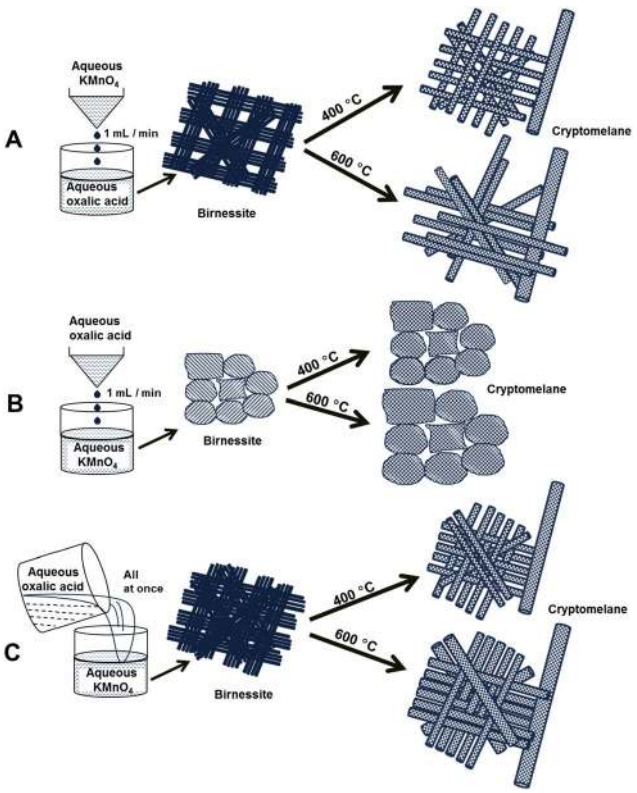

Fig. 12 Schematic of formation of birnessite and cryptomelane nanostructures.

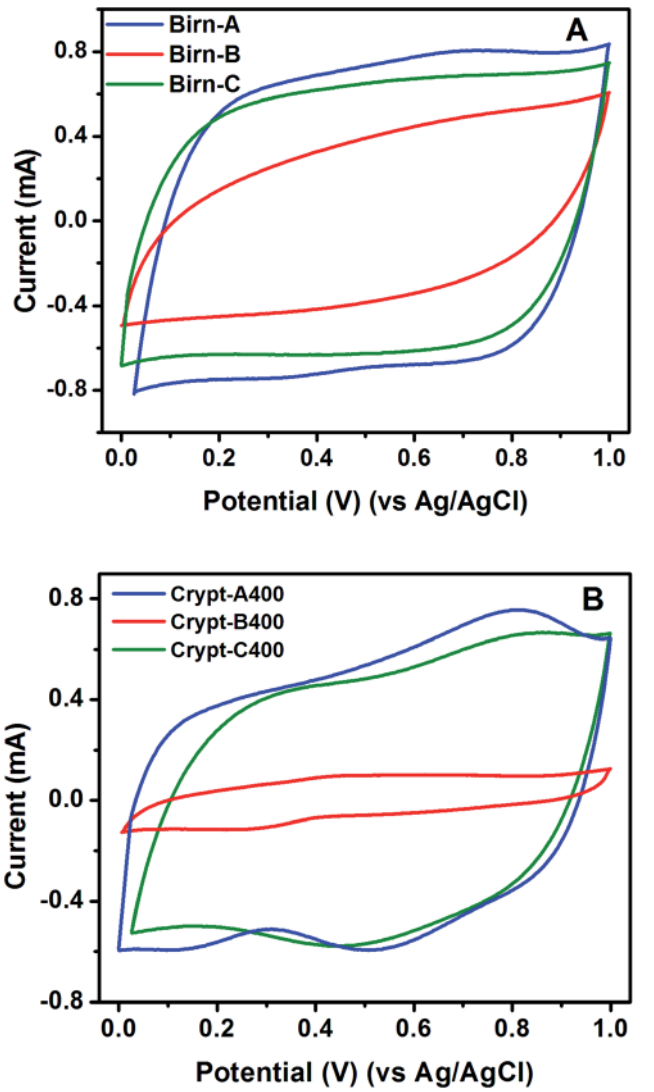

Fig. 13 Cyclic voltammograms of birnessite (A) and cryptomelane (B) carbon composite electrodes, run in 0.1 M aqueous Na_2SO_4 solution at a scan rate of 10 mA s^{-1}.

Charge–discharge cycles of the carbon composites of birnessites and cryptomelanes are given in Fig. 14(A) and (B) respectively. The specific capacitance values of MnO_2–carbon composites were calculated using the formula, $C = I\,\Delta t/\Delta Vm$, where, I is the current, Δt is discharge time of cycle, ΔV is potential window and m is mass of the composite.[20,28,32,55] Linear variation of the charge–discharge curves is observed for the birnessite samples. Specific capacitance values of composites are given in Table 1. Specific capacitance of Ketjen black carbon

Published on 23 July 2014. Downloaded by University of Pittsburgh on 30/10/2014 17:09:27.

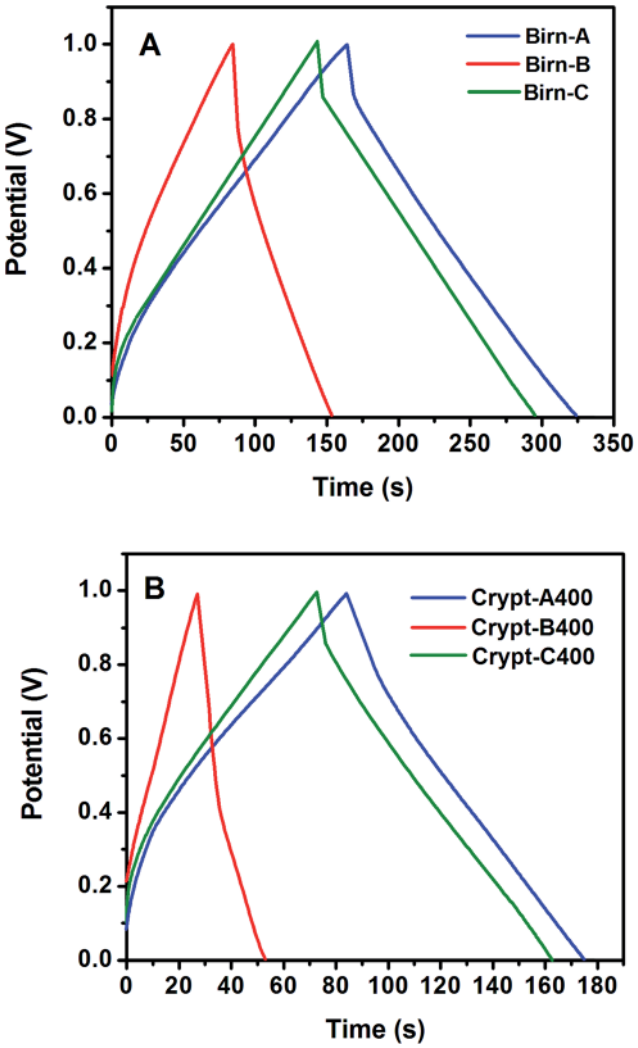

Fig. 14 Galvanostatic charge–discharge curves of birnessite (A) and cryptomelane (B) carbon composite electrodes, run in 0.1 M aqueous Na_2SO_4 solution at a constant current of 0.5 mA.

measured under the similar conditions is only 13 F g^{-1}. Specific capacitance of Birn-A, Birn-B and Birn-C is 234, 113 and 201 F g^{-1} respectively. The highest specific capacitance *i.e.*, 234 F g^{-1}, shown by Birn-A may be attributed to its highest surface area *i.e.*, 202 m^2 g^{-1}. The specific capacitance of A, B and C of cryptomelane analogue is 137, 33 and 128 F g^{-1} respectively. In the case of cryptomelanes also, the same order of capacitance values holds good. In order to ignore the effect of surface area and look into other inherent contributing factors of the electrodes, ratio of specific capacitance (C_s) and specific surface area (SSA) has been calculated and given in Table 1. As for the ratios of C_s/SSA, a trend similar to that of specific capacitance is observed. In addition, the capacitance of the birnessites is found to be higher than that of cryptomelanes except that B (*i.e.*, particles) analogues show similar values. The lower capacitance of Birn-B and Crypt-B400 may be due to their particle morphology which causes probably high electrode resistance. This observation has consistency with the poorly featured CV curve shown by B analogues. On the contrary, A and C analogues are nanowires (having long-range order in one dimension) and those nanowires are interconnected by forming network superstructure so higher conductivities are expected in their cases than B analogues (*i.e.*, nanoparticles). In spite of the fact that electronic conductivity of the cryptomelane is higher than that of birnessites, birnessites show higher capacitance per unit surface area.[25,62] Birnessite samples show better capacitance magnitudes than cryptomelanes even though the former is less crystalline than the latter as per XRD results. Although the crystalline nature of the Crypt-B400 and Crypt-C400 are higher than that of Crypt-A400 as understood from XRD line intensities, Crypt-A400 shows better capacitance values. These observations reveal that crystalline nature of MnO_2 materials does not affect their capacitance significantly. Recently, Boisset *et al.*, have studied the electrochemical performance of Na-Birnessite (synthesized) and cryptomelane (from Erachem-Comilog) electrodes in various lithium salts electrolytes including lithium sulphate using cyclic voltametry.[63] It was found that cryptomelanes with the BET surface area of ~218 m^2 g^{-1} has shown a capacitance of ~163 F g^{-1} in 2 M Li_2SO_4 and Na-birnessite with the BET surface area of ~20 m^2 g^{-1} has shown ~185 F g^{-1} in the same electrolyte.[63,64] Na-birnessite is found to show better capacitance performance than cryptomelane. Results of the current work are in consistent with those observations. Also, the MnO_2 materials synthesized by the oxalate reduction method show better performances.

The observed capacitance values are in agreement with the argument that ionic conductivity is more essential than electronic conductivity for MnO_2 in order for showing high capacity.[25] In fact, ionic conductivity of birnessites is higher than that of cryptomelanes. The present study reveals that besides crystal structure, crystalline nature and surface area, ionic conductivity and morphology of the electrode materials are key factors in determining their capacitance values. Stability of the capacitance of the samples estimated based on the charge–discharge curves is provided in Fig. 15. Loss of

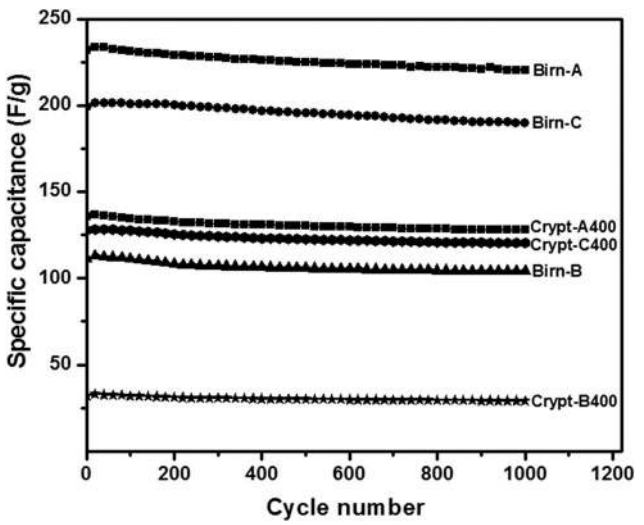

Fig. 15 Variation of specific capacitance with charge–discharge cycle number.

This journal is © The Royal Society of Chemistry 2014

Published on 23 July 2014. Downloaded by University of Pittsburgh on 30/10/2014 17:09:27.

capacitance after 1000 cycles for birnessites (A, B and C) is 6, 7.9 and 5.5% and for cryptomelanes (A, B and C) is 6.7, 12.1 and 6.1%, respectively. Stability results of the K–MnO_2 samples imply that these samples show good stability and that birnessite samples show better stability than cryptomelane samples. In the case of both birnessites and ctyptomelanes, capacitance values for A and C analogues are more stable than B analogues. This might be due to the particle morphology of the B analogues. The better stability exhibited by the C analogues over the A analogues might be due to the rigid, hierarchical superstructure (formed with nanowires network) of the former. Hence, birnessites (A and C) synthesized by the current method can be promising and cost-effective materials for capacitor applications.

4. Conclusions

Amorphous birnessite samples with different morphologies (nanorods network, nanoparticles and gel-type) and textural properties have been synthesized using $KMnO_4$ and oxalic acid solutions at mild conditions by altering the rate and the order of mixing the reactants at ambient conditions. One of the birnessites formed with the slow addition of $KMnO_4$ to oxalic acid showed BET surface area of as high as 202 $m^2\ g^{-1}$. Calcination of as-synthesized birnessites at $\geq$400 °C for 4 h in air has led to the formation of cryptomelane samples with similar morphologies. A gel-type MnO_2 formed shows mesoporous nature with a narrow pore size distribution (centered at $\sim$50 Å) and hence it can be exploited for applications requiring specific pore size. The pH of the reaction medium has been found to be responsible for the formation of MnO_2 with different features.

Electrochemical capacitance of MnO_2–carbon black composites has been studied by CV curves and charge–discharge cycling. The specific capacitance values of MnO_2 samples were found to have a direct relation with their specific surface area. One of the birnessite samples showed a specific capacitance (C_s) as high as 234 F g^{-1} and exhibit better capacitance behavior than its cryptomelane counterpart. Nanowires of MnO_2 exhibited higher capacitance than nanoparticles. Thus, the present study suggests that textural properties, crystal structure, morphology and ionic conductivity govern the capacitance of MnO_2-based electrode materials. These MnO_2-based electrodes showed good stability over 1000 charge–discharge cycles. Thus, the present study suggests that Birn-A and Birn-C can be the cost-effective and promising electrode materials for capacitors.

Acknowledgements

The Department of Science and Technology (Government of India) is gratefully acknowledged for funding NCCR. We acknowledge (Late) Prof. Ramprasad Viswanath for his contribution to this work.

Notes and references

1 A. C. Dillon, *Chem. Rev.*, 2010, **110**, 6856–6872.
2 I. Hadjipaschalis, A. Poullikkas and V. Efthimiou, *Renewable Sustainable Energy Rev.*, 2009, **13**, 1513–1522.
3 Z. S. Wu, K. Parvez, X. Feng and K. Müllen, *Nat. Commun.*, 2013, **4**, 2487.
4 C. Yuan, L. Hou, D. Li, L. Yang and J. Li, *Int. J. Electrochem.*, 2012, **2012**, 714092.
5 S. Vijayakumar, S. Nagamuthu and G. Muralidharan, *ACS Appl. Mater. Interfaces*, 2013, **5**, 2188–2196.
6 M. B. Zheng, J. Cao, S. T. Liao, J. S. Liu, H. Q. Chen, Y. Zhao, W. J. Dai, G. B. Ji, J. M. Cao and J. Tao, *J. Phys. Chem. C*, 2009, **113**, 3887–3894.
7 Y. Luo, J. Jiang, W. Zhou, H. Yang, J. Luo, X. Qi, H. Zhang, D. Y. W. Yu, C. M. Li and T. Yu, *J. Mater. Chem.*, 2012, **22**, 8634–8640.
8 W. C. Fang, *J. Phys. Chem. C*, 2008, **112**, 11552–11555.
9 R. Ganesan, I. Perelshtein and A. Gedanken, *J. Phys. Chem. C*, 2008, **112**, 1913–1919.
10 L. Can, L. Zhengcao and Z. Zhengjun, *Sci. Technol. Adv. Mater.*, 2013, **14**, 065005.
11 J. Rajeswari, P. S. Kishore, B. Viswanathan and T. K. Varadarajan, *Electrochem. Commun.*, 2009, **11**, 572–575.
12 R. Jothiramalingam, B. Viswanathan and T. K. Varadarajan, *Catal. Commun.*, 2005, **6**, 41–45.
13 Q. H. Zhang, S. Y. Sun, S. P. Li, H. Jiang and J. G. Yu, *Chem. Eng. Sci.*, 2007, **62**, 4869–4874.
14 Y. F. Shen, R. P. Zerger, R. N. Deguzman, S. L. Suib, L. Mccurdy, D. I. Potter and C. L. Oyoung, *Science*, 1993, **260**, 511–515.
15 J. J. Yu, T. Zhao and B. Z. Zeng, *Electrochem. Commun.*, 2008, **10**, 1318–1321.
16 F. Y. Cheng, J. Z. Zhao, W. Song, C. S. Li, H. Ma, J. Chen and P. W. Shen, *Inorg. Chem.*, 2006, **45**, 2038–2044.
17 W. F. Wei, X. W. Cui, W. X. Chen and D. G. Ivey, *Chem. Soc. Rev.*, 2011, **40**, 1697–1721.
18 W. Xiao, D. L. Wang and X. W. Lou, *J. Phys. Chem. C*, 2010, **114**, 1694–1700.
19 B. A. Pinaud, Z. Chen, D. N. Abram and T. F. Jeramilo, *J. Phys. Chem. C*, 2011, **115**, 11830–11838.
20 L. Athouel, F. Moser, R. Dugas, O. Crosnier, D. Belanger and T. Brousse, *J. Phys. Chem. C*, 2008, **112**, 7270–7277.
21 M. Toupin, T. Brousse and D. Belanger, *Chem. Mater.*, 2004, **16**, 3184–3190.
22 Y. T. Wang, A. H. Lu, H. L. Zhang and W. C. Li, *J. Phys. Chem. C*, 2011, **115**, 5413–5421.
23 S. Devaraj and N. Munichandraiah, *J. Phys. Chem. C*, 2008, **112**, 4406–4417.
24 T. Brousse, M. Toupin, R. Dugas, L. Athouel, O. Crosnier and D. Belanger, *J. Electrochem. Soc.*, 2006, **153**, A2171–A2180.
25 O. Ghodbane, J. L. Pascal and F. Favier, *ACS Appl. Mater. Interfaces*, 2009, **1**, 1130–1139.
26 W. F. Wei, X. W. Cui, W. X. Chen and D. G. Ivey, *J. Phys. Chem. C*, 2008, **112**, 15075–15083.
27 M. Xu, L. Kong, W. Zhou and H. Li, *J. Phys. Chem. C*, 2007, **111**, 19141–19147.
28 Y. Ma, J. Luo and S. L. Suib, *Chem. Mater.*, 1999, **11**, 1972–1979.
29 S. Ching, J. L. Roark, N. Duan and S. L. Suib, *Chem. Mater.*, 1997, **9**, 750–754.

Published on 23 July 2014. Downloaded by University of Pittsburgh on 30/10/2014 17:09:27.

30 C. C. Chen, D. C. Golden and J. B. Dixon, *Clays Clay Miner.*, 1986, **34**, 565–571.
31 Q. Feng, H. Kanoh, Y. Miyai and K. Ooi, *Chem. Mater.*, 1995, **7**, 1226–1232.
32 R. J. Chen, P. Zavalij and M. S. Whittingham, *Chem. Mater.*, 1996, **8**, 1275–1280.
33 A. C. Gaillot, D. Flot, V. A. Drits, A. Manceau, M. Burghammer and B. Lanson, *Chem. Mater.*, 2003, **15**, 4666–4678.
34 S. L. Brock, N. G. Duan, Z. R. Tian, O. Giraldo, H. Zhou and S. L. Suib, *Chem. Mater.*, 1998, **10**, 2619–2628.
35 P. Ragupathy, D. H. Park, G. Campet, H. N. Vasan, S. J. Hwang, J. H. Choy and N. Munichandraiah, *J. Phys. Chem. C*, 2009, **113**, 6303–6309.
36 D. Frias, S. Nousir, I. Barrio, M. Montes, T. Lopez, M. A. Centeno and J. A. Odriozola, *Mater. Charact.*, 2007, **58**, 776–781.
37 H. Cao and S. L. Suib, *J. Am. Chem. Soc.*, 1994, **116**, 5334–5342.
38 D. Portehault, S. Cassaignon, E. Baudrin and J. P. Jolivet, *Chem. Mater.*, 2007, **19**, 5410–5417.
39 M. Villalobos, B. Lanson, A. Manceau, B. Toner and G. Sposito, *Am. Mineral.*, 2006, **91**, 489–502.
40 H. T. Zhu, J. Luo, H. X. Yang, J. K. Liang, G. H. Rao, J. B. Li and Z. M. Du, *J. Phys. Chem. C*, 2008, **112**, 17089–17094.
41 B. E. Warren, *Phys. Rev.*, 1941, **59**, 693–698.
42 R. M. McKenzie, *Mineral. Mag.*, 1971, **38**, 493–502.
43 J. C. Villegas, O. H. Giraldo, K. Laubernds and S. L. Suib, *Inorg. Chem.*, 2003, **42**, 5621–5631.
44 Q. H. Zhang, J. Luo, E. Vileno and S. L. Suib, *Chem. Mater.*, 1997, **9**, 2090–2095.
45 O. Prieto, M. Del Arco and V. Rives, *J. Mater. Sci.*, 2003, **38**, 2815–2824.
46 J. E. Post and D. R. Veblen, *Am. Mineral.*, 1990, **75**, 477–489.
47 R. L. Penn and J. F. Banfield, *Science*, 1998, **281**, 969–971.
48 E. K. Nyutu, C. H. Chen, S. Sithambaram, V. M. B. Crisostomo and S. L. Suib, *J. Phys. Chem. C*, 2008, **112**, 6786–6793.
49 K. S. W. Sing, D. H. Everett, R. A. W. Haul, L. Moscou, R. A. Pierotti, J. Rouquerol and T. Siemieniewska, *Pure Appl. Chem.*, 1985, **57**, 603–619.
50 G. Milazzo, S. Caroli and V. K. Sharma, *Tables of Standard Electrode Potentials*, Wiley, New York, 1978.
51 S. Navaladian, C. M. Janet, B. Viswanathan, T. K. Varadarajan and R. P. Viswanath, *J. Phys. Chem. C*, 2007, **111**, 14150–14156.
52 S. Navaladian, B. Viswanathan, R. P. Viswanath and T. K. Varadarajan, *Nanoscale Res. Lett.*, 2007, **2**, 44–48.
53 V. Pimienta, D. Lavabre, G. Levy and J. C. Micheau, *J. Phys. Chem.*, 1994, **98**, 13294–13299.
54 L. X. Yang, Y. J. Zhu and G. F. Cheng, *Mater. Res. Bull.*, 2007, **42**, 159–164.
55 D. Portehault, S. Cassaignon, E. Baudrin and J. P. Jolivet, *Chem. Mater.*, 2008, **20**, 6140–6147.
56 V. Subramanian, H. W. Zhu, R. Vajtai, P. M. Ajayan and B. Q. Wei, *J. Phys. Chem. B*, 2005, **109**, 20207–20214.
57 S. Devaraj and N. Munichandraiah, *J. Electrochem. Soc.*, 2007, **154**, A80–A88.
58 V. Subramanian, H. W. Zhu and B. Q. Wei, *J. Power Sources*, 2006, **159**, 361–364.
59 P. Ragupathy, H. N. Vasan and N. Munichandraiah, *J. Electrochem. Soc.*, 2008, **155**, A34–A40.
60 D.-Y. Sung, I. Y. Kim, T. W. Kim, M.-S. Song and S.-J. Hwang, *J. Phys. Chem. C*, 2011, **115**, 13171–13179.
61 C. C. Hu and T. W. Tsou, *Electrochem. Commun.*, 2002, **4**, 105–109.
62 S. L. Suib, *Acc. Chem. Res.*, 2008, **41**, 479–487.
63 A. Boisset, L. Athouël, J. Jacquemin, P. Porion, T. Brousse and M. Anouti, *J. Phys. Chem. C*, 2013, **117**, 7408–7422.
64 L. Athouël, P. Arcidiacono, C. Ramirez-Castro, O. Crosnier, C. Hamel, Y. Dandeville, P. Guillemet, Y. Scudeller, D. Guay, D. Bélanger and T. Brousse, *Electrochim. Acta*, 2012, **86**, 268–276.

 This journal is © The Royal Society of Chemistry 2014